Viscoelastic mechanical characterization of a short-fiber reinforced polyethylene tube: Experiments and modelling

Diego Celentano [a], *, Danilo Wimmer [a], Lucas Colabella [b], Adrián P. Cisilino [b]

[a] Departamento de Ingeniería Mecánica y Metalúrgica, Pontificia Universidad Católica de Chile, Avda. Vicuña Mackenna 4860, Santiago de Chile, Chile
[b] División Mecánica de Materiales, INTEMA, Facultad de Ingeniería — CONICET, Universidad Nacional de Mar del Plata, Av. Juan B. Justo 4302, 7600 Mar del Plata, Argentina

ARTICLE INFO

ABSTRACT

It is presented in this paper a characterization of the viscoelastic mechanical response of short-fiber reinforced thermoplastic tubes. The tubes are manufactured by helical winding of a composite made of high-density polyethylene with short glass-fibers as reinforcement. The mechanical behavior of the composite lamina is characterized by means of monotonic and loading/unloading tensile tests at different deformation rates for specimens extracted in the axial and circumferential directions of the tube. Based on the experimental results, a three-dimensional Maxwell model with eight parameters, five to describe the elastic anisotropy response and three to describe the incompressible-isotropic visco-plastic response, is proposed. The comparison of the model results with the experimental data shows that the model properly captures the material non-linear anisotropic behavior. The only exception is the unloading of the specimens in the circumferential direction, for which the final deformation after the complete unloading is largely overestimated. The model is implemented as part of a finite element code and validated by comparison to experimental measurements of a full-scale test that combines the bending and punching of a tube. The proposed non-linear model for the reinforced polyethylene constitutes a step forward with respect to the classical linear-elastic analysis used for tubes.

© 2015 Elsevier Ltd. All rights reserved.

1. Introduction

The use of thermoplastics in the industry has been growing considerably thanks to their good and versatile properties and low cost in relation with others materials. These wide ranges of properties are due to many factors: chemical composition (e.g. polyethylene and polypropylene), polymerization conditions (e.g. high and low density polyethylene) and manufacturing methods (e.g. extrusion and molding), among others. Furthermore, thermoplastic matrices can be combined with fiber reinforcements (e.g. glass, carbon, aramid, etc.) to produce composite materials with outstanding mechanical properties.

Short-fiber reinforced plastics present, in general, some isotropy that depends on the fiber orientation. Typically, reinforced plastics are considered to be transversally isotropic in the case the fibers are unidirectional; or isotropic when the fibers are randomly oriented. The mechanical responses of the reinforced plastics combine non-linear elastic, inelastic and strain-rate sensitive behaviors. Such complex behaviors make reinforced plastics difficult to characterize, and due to this, they constitute a busy topic of research [1—5].

A number of approaches are proposed to model the mechanical behaviors of fiber-reinforced materials. In what respect to the elastic behavior, the simplest models are the series, parallel, Hirch, Halpin-Tsai, modified Halpin-Tsai, Cox and modified Bowyer and Bader. Although these models have been extensively applied, it was found that they are only useful to estimate some tensile properties [1—5]. More general elastic models include a distribution function for the fiber orientations. In particular, Hamed et al. [8] introduce a method for the elastic characterization of angle-ply laminate and filament wound tubes. These models can represent the anisotropy but not the viscoelastic behavior [6,7]. One of the simplest models that incorporate viscoelastic behavior is that due to Maxwell, which has the elastic and viscous elements in series. Maxwell models allow predicting viscoelastic responses with quite close agreements to experimental results [9—13]. Nevertheless, due to the many parameters involved, Maxwell models are difficult to implement and to calibrate, and thus its industrial applicability is limited.

* Corresponding author.
E-mail address: dcelentano@ing.puc.cl (D. Celentano).

This paper addresses the characterization of the viscoelastic mechanical response of short-fiber reinforced thermoplastic tubes. The tubes are manufactured by helical winding of a composite made of high-density polyethylene (HDPE) with short glass-fibers as reinforcement.

These tubes can be used for a variety of different applications including mining tailings transport, submarine outfalls, pipelines in roads and drains. A material model is developed based on experimental data. The model is implemented as part of a finite element code, which is validated by comparison to measurements practiced as part of full-scale test that combines the bending and punching of a tube. This test mimics loading conditions that usually occur during the installation, assembly and service of the tubes.

2. Material characterization

2.1. Material and methods

The material under study is a reinforced polyethylene provided by Krah Chile [14]. The reinforcement consists in 20% in-weight of short glass-fibers. The fibers were manufactured by extrusion followed by wire drawing. Their average diameter is 10 μm and they are 3 mm long. The specimens were obtained from a helically wounded 1000-mm-diameter tube. The tube was fabricated using three 6-mm-thick laminas with the stacking sequence $[-\varphi,+\varphi,-\varphi]$, being $\varphi = 82°$ measured with respect to the longitudinal direction of the tube, x_1, see Fig. 1a. The laminas were obtained from extrusion and, therefore, the fiber should orientate preferentially in the flow direction [15,16]. The direction of the fiber orientation is denoted as ξ_1 in the lamina system of coordinates, see Fig. 1b.

Tensile tests were performed using type-I specimens in accordance to ASTM D638 [17]. The dimensions of the calibrated section of the specimens were 6 mm and 12 mm. Three sets of specimens were extracted from the middle zone of the tube thickness: longitudinal specimens with their widths in the circumferential direction (specimens labeled as LC), circumferential specimens with their widths in the longitudinal direction (specimens labeled as CL) and longitudinal specimens with their widths in the radial direction (specimens labeled as LR). Note that, consistently with the specimen width, the LC and CL specimens spread over a single lamina (that oriented $+\varphi$), whereas the LR specimens spread over three laminas (this is, half the lamina oriented $-\varphi$, the complete lamina oriented $+\varphi$, and half the lamina oriented $-\varphi$). The assumption on the preferential orientation of the fibers was confirmed by SEM observations. Specimens were taken from the fracture surfaces, gold plated and observed with a JEOL JSM 5300 (Jeol Ltd., Tokyo, Japón) equipped with the ADDA II interface and the AnalySIS software. The picture in Fig. 2 for the fracture surface of a LC specimen clearly shows the preferential orientation of the fibers.

The specimen deformations were measured by means of clip-gauge extensometer and digital image correlation (DIC). Complementary verification measurements of the evolution of the specimen width during the test were done using a manual electronic caliper. A 2630 Series Instron static clip-on extensometer was used to measure the longitudinal deformation. DIC measurements were performed using an in-house developed set-up based on a Canon EOS Rebel XSI 12.2-megapixel digital camera and the displacement correlation and tracking software due to Eberl [18]. This software uses the zero-normalized cross-correlation criterion [19] and reaches a sub-pixel resolution using peak-finding algorithm [20]. The software capabilities were extended to compute the strains via the differentiation of the displacement fields by means of a point-wise least squares algorithm [21]. The caliper was a Series 500 Mitutoyo.

Specimens LC and CL were subjected to monotonic tensile load up to rupture, and to loading/unloading cycles. The tests were carried out by controlling the crosshead speed displacement. Three velocities were used, $v = 0.1$, 1 and 10 mm/min. Three specimens were test in each case. All the specimens were instrumented with the clip-gauge extensometer to measure the longitudinal deformation. Extra sets of LC and LR specimens were tested in tension at $v = 1$ mm/min while monitored with the DIC. The DIC data was used to retrieve the Poisson's ratios. The computation of the Poisson's ratios using a single set of data is sustained on the evidence about the independence of this material property with the deformation rate [22].

2.2. Results

2.2.1. Monotonic tensile tests up to rupture

The average stress-strain responses of the LC and CL specimens for the three crosshead-velocities are shown in Fig. 3. The maximum standard errors for the stresses measurements are 2 MPa and 5 MPa for the longitudinal and transversal specimens, respectively.

As it was expected, the maximum values for the strength and stiffness are in the circumferential direction, which is closer to the orientation of the fibers. The elastic compliances of the specimens (the slope of the stress-strain curves at zero strain) are found independent of the deformation rate. The uniaxial stiffness for the longitudinal and circumferential specimens are $C_{11}^{exp} = 2.52$ MPa and $C_{22}^{exp} = 4.7$ MPa, respectively. The errors are estimated in 10% for both cases.

The tensile strength increases with the strain-rate. This behavior is in coincidence to those reported by other authors [23,24].

The results for the Poisson's ratios as a function of strain are shown in Figs. 4–6. Fig. 4 shows the results for the Poisson's ratio v_{13}, which were computed using the strain data of the LR experiments. A very good agreement can be observed between the results from the DIC and the caliper. The difference between the two sets of results is of the same order of data dispersion among the specimens. Figs. 5 and 6 present the results for v_{21} and v_{12}, which were computed using the data from CL and LC tests, respectively.

2.2.2. Loading/unloading tests

Fig. 7 shows the average cyclic stress–strain curves of the LC specimens, which were loaded up to 1200 N and then unloaded. Similarly, Fig. 8 shows the stress-strain responses for the CL specimens. In this case, the specimens were loaded up to 4000 N and then unloaded. The maximum standard errors of the measurements are the same of those reported for the monotonic tensile tests.

Figs. 7 and 8 clearly exhibit the hysteresis of the material due to its viscous behavior. It can be observed that the higher the strain-rate, the lower the hysteresis. Besides, the hysteresis is larger in the transversal than in the longitudinal direction. The dependency of the stress rate $\dot{\sigma}$ with the stress σ is shown in Figs. 9 and 10, which were computed from the results in Figs. 7 and 8, respectively. It can be observed that exist acceptable linear relationships between the two variables.

The above result suggests that the material response can be assimilated to that of a Maxwell series model [9],

$$\dot{e}_{ii} = \frac{de_{ii}^{D}}{dt} + \frac{de_{ii}^{S}}{dt} = \frac{\sigma_{ii}}{\eta_i} + \frac{\dot{\sigma}_{ii}}{C_{ii}} , \tag{1}$$

where $\dot{e}$ is the total strain rate and de^{S}/dt and de^{D}/dt are its viscous and elastic components, respectively. The symbol η denotes the viscosity.
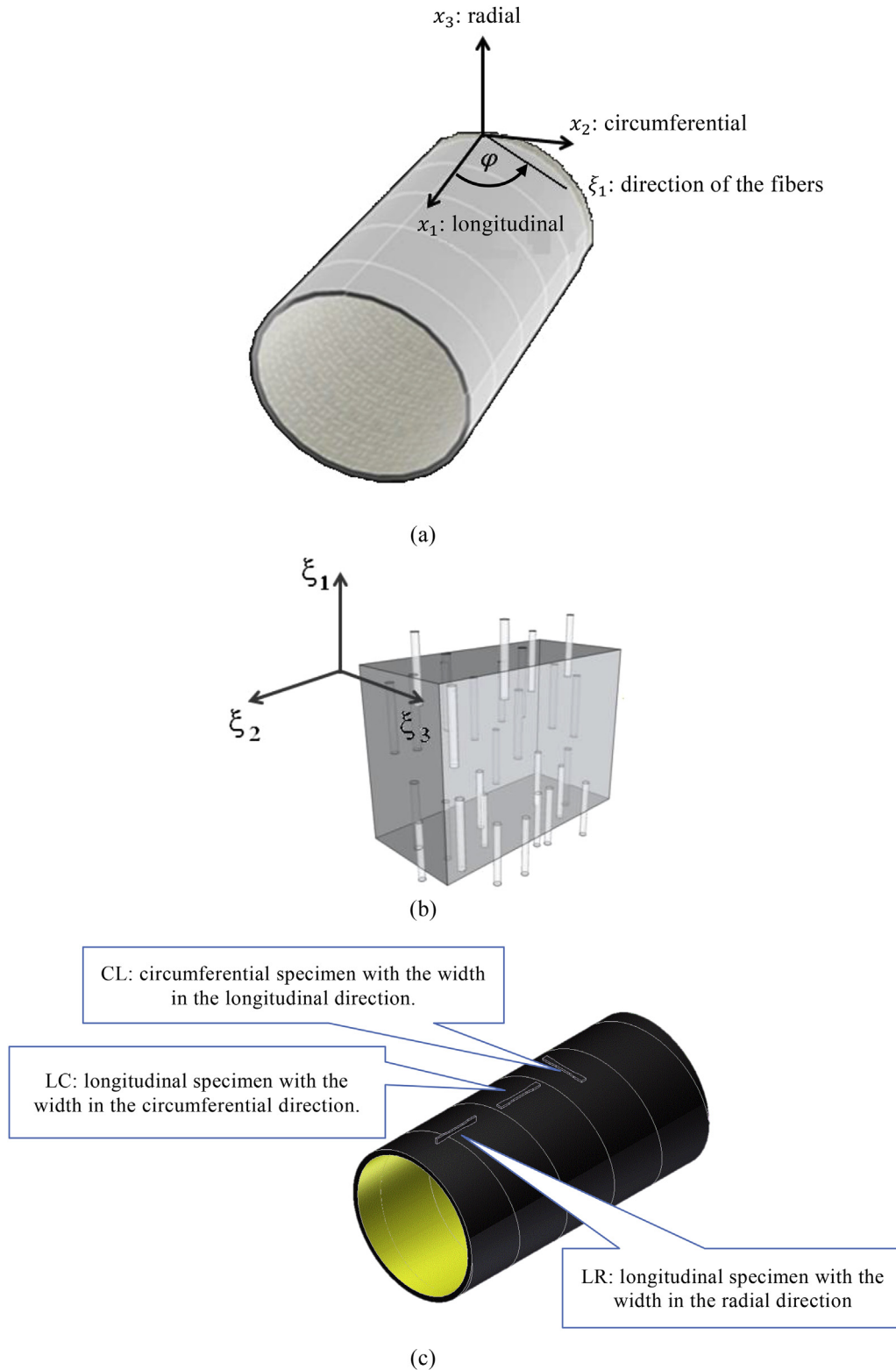
x_3: radial

x_2: circumferential

ξ_1: direction of the fibers

φ

x_1: longitudinal

(a)

ξ_1

ξ_2

ξ_3

(b)

CL: circumferential specimen with the width in the longitudinal direction.

LC: longitudinal specimen with the width in the circumferential direction.

LR: longitudinal specimen with the width in the radial direction

(c)

Fig. 1. a) Global coordinate system for the tube, b) local coordinate systems for the transversal isotropic lamina, and c) locations of the specimens.

Data fitting using the one-dimensional Maxwell model in (1) allowed obtaining a unique linear ln–ln correlation between the viscosity and the total strain-rate for both, the longitudinal and the circumferential specimens. This result is plotted in Fig. 11.

3. Constitutive model

Based on the experimental results in Section 2, it is proposed here to describe the behavior of the composite using a three-dimensional Maxwell model. The model is tailored to account for
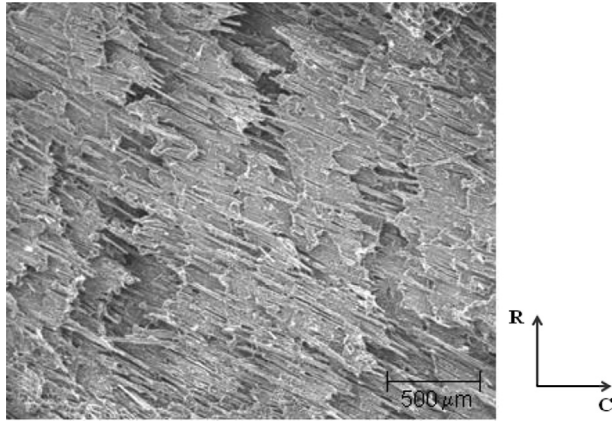
Fig. 2. SEM image (magnification ×35, voltage 20 kV) of the fracture surface of a longitudinal specimen showing the uniform orientation of the fibers.
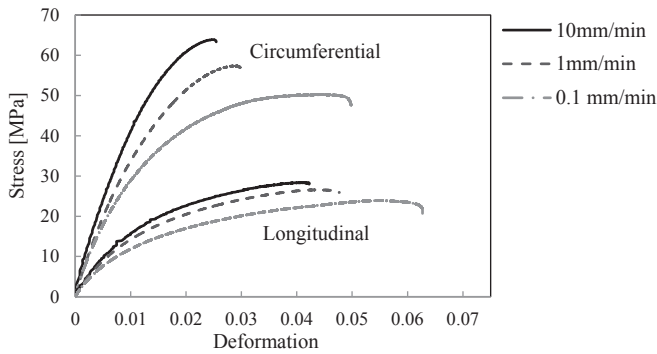

Fig. 3. Mechanical behavior of LC and CL specimens subjected to tension at different crosshead velocities.
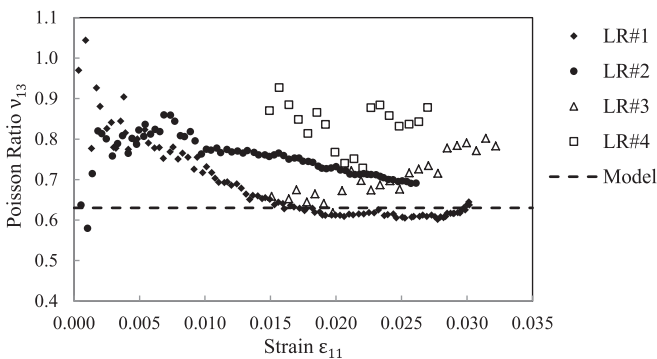

Fig. 4. Results for the Poisson's ratio v_{13} computed using the strain results of the LR specimens. Open symbols are for data measured using the electronic caliper and closed symbols using DIC.
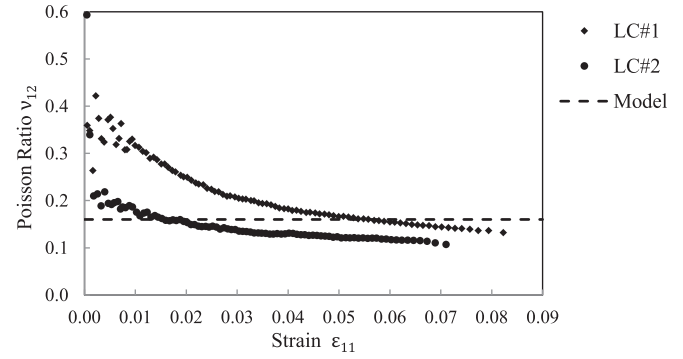

Fig. 5. Results for the Poisson's ratio v_{12} computed using the strain results of the LC specimens. Data measured using DIC.
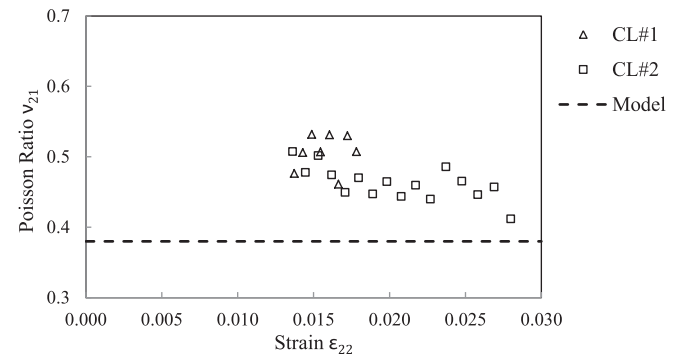

Fig. 6. Results for the Poisson's ratio v_{21} computed using the strain results of the CL specimens. Data measured using the electronic caliper.

the elastic anisotropy while the viscous behavior is specified using an incompressible-isotropic viscoplastic Newton flow.

3.1. Stress–strain law

The following stress–strain relationship is adopted [25]:

$$\boldsymbol{\sigma} = \boldsymbol{C} : (\boldsymbol{e} - \boldsymbol{e}^v), \tag{2}$$

where $\boldsymbol{\sigma}$ is the Cauchy stress tensor, $\boldsymbol{C}$ is the elastic constitutive tensor and $\boldsymbol{e} = \frac{1}{2}(1 - \boldsymbol{F}^T\boldsymbol{F}^{-1})$ is the Almansi strain tensor with $\boldsymbol{F}$ being

the deformation gradient tensor. The superscript v stands for the viscous component of the deformation.

The evolution of the internal variable $\boldsymbol{e}^v$ is defined within the associate rate-dependent viscoplasticity theory context as

$$L_v(\boldsymbol{e}^v) = \lambda\left(\frac{\partial F}{\partial \boldsymbol{\sigma}}\right), \tag{3}$$

where L_v is the Lie derivative (frame-indifferent), λ is the viscoplastic parameter, and $F(\boldsymbol{\sigma})$ is the plastic flow potential. Pure viscoelasticity is recovered by assuming:

$$\lambda = \frac{F}{\eta}, \tag{4}$$

together with

$$F = \sigma_{eq} = \sqrt{3J_2} \geq 0, \tag{5}$$

where σ_{eq} is the von Mises equivalent stress and $J_2 = \frac{1}{2}(\boldsymbol{\sigma'}:\boldsymbol{\sigma'})$ is the second invariant of the deviatoric stress, $\boldsymbol{\sigma'} = \boldsymbol{\sigma} - p\boldsymbol{I}$, with $\boldsymbol{I}$ being the identity tensor and $p = 1/3tr(\boldsymbol{\sigma})$ the pressure with $tr(\cdot)$ being the trace operator.

3.2. Transversal isotropic elastic response

The elastic response of the lamina is assumed to be transversally isotropic, with the plane of isotropy, $\xi_2\xi_3$, perpendicular to the direction of the fibers, ξ_1 (see Fig. 1b). Thus, the lamina compliance matrix in the local coordinate system expressed in the Voigt notation is
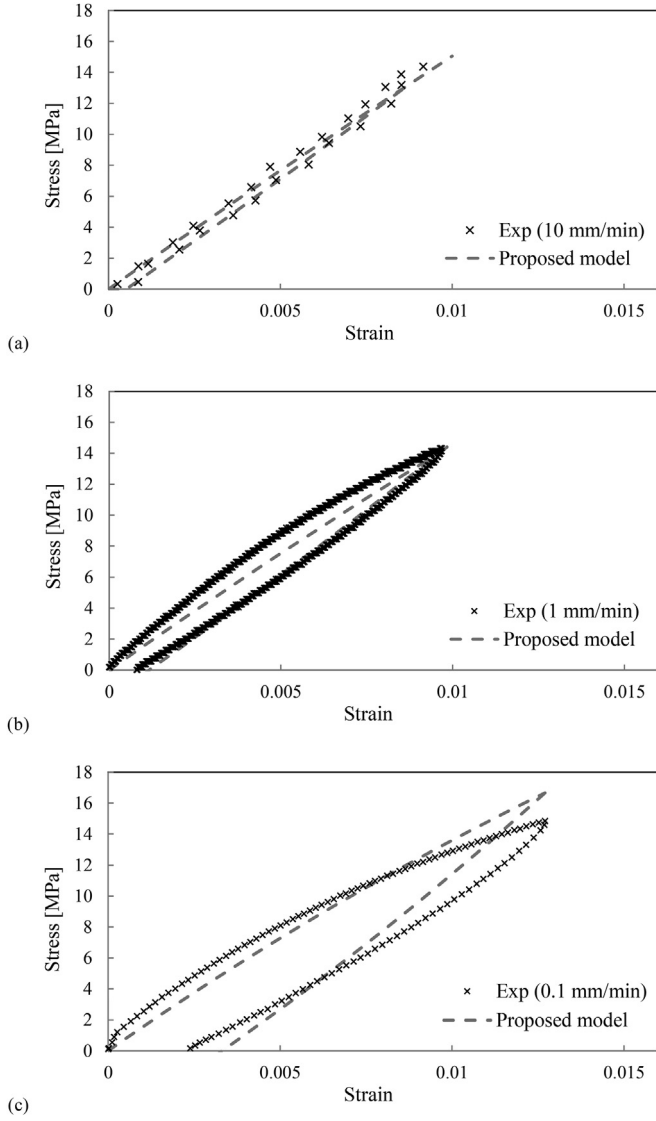
Fig. 7. Mechanical behavior of LC specimens subjected to cyclic test at a) 10 mm/min, b) 1 mm/min and c) 0.1 mm/min crosshead velocities.
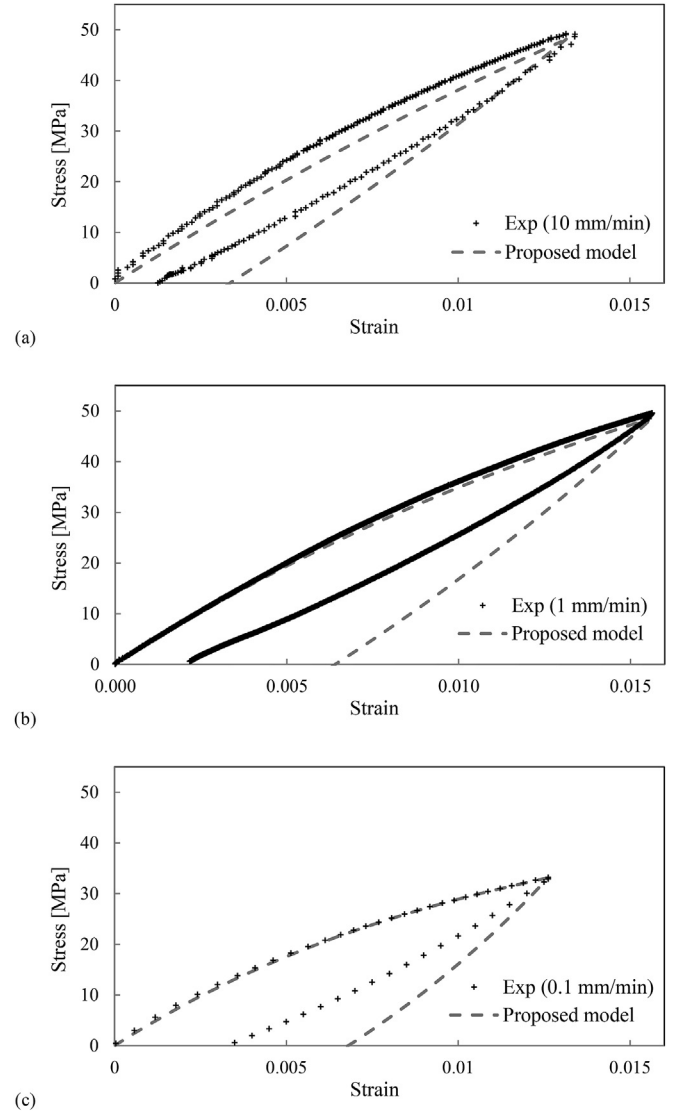

Fig. 8. Mechanical behavior of CL specimens subjected to cyclic test to a) 10 mm/min, b) 1 mm/min and c) 0.1 mm/min crosshead velocities.

$$
\boldsymbol{D}' = \begin{bmatrix}
\dfrac{1}{E'_{11}} & -\dfrac{\nu'_{21}}{E'_{22}} & -\dfrac{\nu'_{21}}{E'_{22}} & 0 & 0 & 0 \\[2mm]
-\dfrac{\nu'_{12}}{E'_{11}} & \dfrac{1}{E'_{22}} & -\dfrac{\nu'_{23}}{E'_{22}} & 0 & 0 & 0 \\[2mm]
-\dfrac{\nu'_{12}}{E'_{11}} & -\dfrac{\nu'_{23}}{E'_{22}} & \dfrac{1}{E'_{22}} & 0 & 0 & 0 \\[2mm]
0 & 0 & 0 & \dfrac{(1+\nu'_{23})}{E'_{22}} & 0 & 0 \\[2mm]
0 & 0 & 0 & 0 & \dfrac{1}{2G'_{12}} & 0 \\[2mm]
0 & 0 & 0 & 0 & 0 & \dfrac{1}{2G'_{12}}
\end{bmatrix}
\tag{6}
$$

where E'_{ii}, G'_{ij} and ν'_{ij} are the lamina Young's moduli, shear moduli and Poisson's ratios, respectively (note that only five elastic constants are necessary to describe a transversely isotropic material).

The elastic constitutive tensor is the inverse of the compliance matrix, $\boldsymbol{C}' = \boldsymbol{D}'^{-1}$, which can be transformed to the tube coordinate system using standard procedures for fourth-order tensors,

$$
C_{pqrs} = A_{pj}A_{qk}A_{rl}A_{rm}C'_{jklm},
\tag{7}
$$

where $\boldsymbol{A}$ is the rotation matrix, which for the present case is

$$
\boldsymbol{A} = \begin{bmatrix}
\cos(\theta) & -\sin(\theta) & 0 \\
\sin(\theta) & \cos(\theta) & 0 \\
0 & 0 & 1
\end{bmatrix},
\tag{8}
$$

where $\theta = +\varphi, -\varphi$ depending on the lamina being considered (see Section 3.1).

3.3. Viscous response

Based on the results in Section 2.2.2, the viscous response is assumed isotropic with the viscosity η being a function of the strain-rate with the following expression:
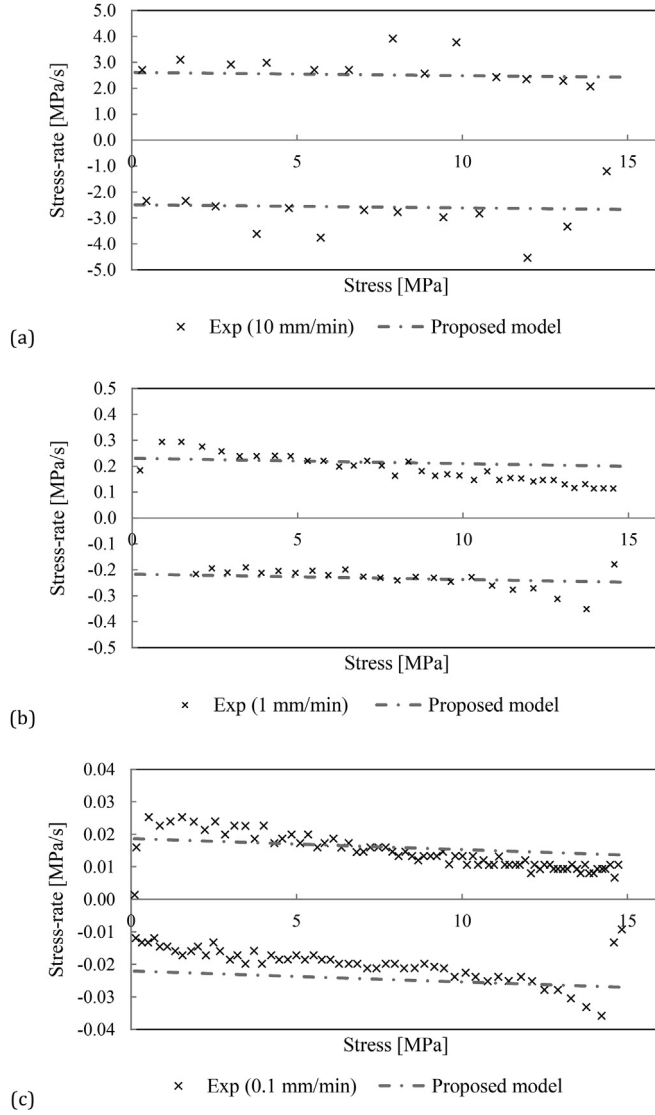
(a)

(b)

(c)

Fig. 9. Stress-rate versus stress for the LC specimens at a) 10 mm/min, b) 1 mm/min and c) 0.1 mm/min crosshead velocities.

(a)

(b)

(c)

Fig. 10. Stress-rate versus stress for the CL specimens at a) 10 mm/min, b) 1 mm/min and c) 0.1 mm/min crosshead velocities.

$$\eta(\dot{e}_{eq}) = He^{-b\,\ln\,\dot{e}_{eq}} \le \eta_{max}, \qquad (9)$$

where H and b are material parameters, η_{max} is a cut-off value aimed at describing the viscous response for nearly zero strain-rates and $\dot{e}_{eq}$ is the equivalent strain-rate which, in this context, is defined as:

$$\dot{e}_{eq} = \frac{\boldsymbol{\sigma} : L_v(\boldsymbol{e})}{\sigma_{eq}}. \qquad (10)$$

3.4. Estimation of the constitutive material constants

Assuming that $\dot{e}$ is constant in the tensile tests shown in Section 2, we retrieve the Maxwell model in equation (1), which can be rewritten as:

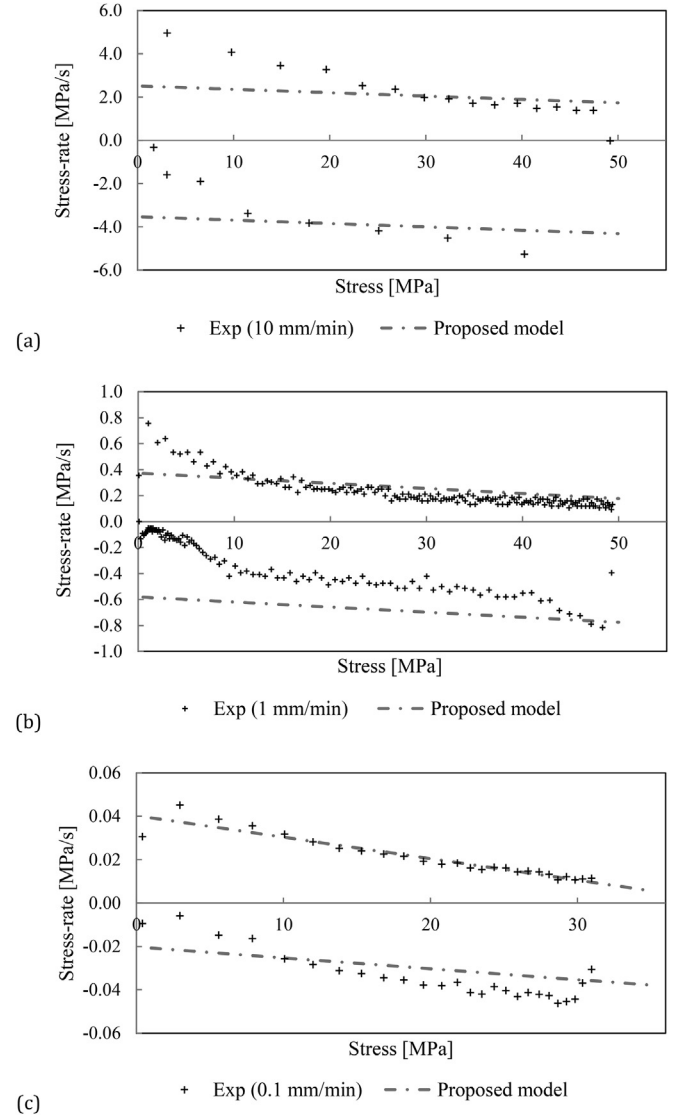$$\dot{\sigma}_{ii} = -\frac{C_{ii}}{\eta}\sigma_{ii} + C_{ii}\dot{e}. \qquad (11)$$

The main feature of equation (11) is the linear relationship between $\dot{\sigma}$ and σ, which does not depend on the initial strain. Then, by adopting the ln–ln relationship between viscosity and strain-
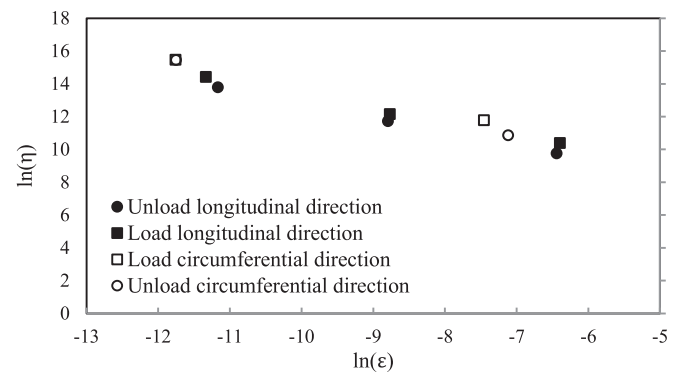

Fig. 11. Linear ln–ln relation between the viscosity and the total strain-rate in the longitudinal and circumferential directions.

rate in equation (9), and the compliance matrix of the lamina C, the uniaxial stress tensile responses for longitudinal and circumferential specimens can be described using

$$\dot{\sigma}_{11} = -C_{11} \frac{\sigma_{11}}{H e^{-b \ln \dot{e}_{eq}}} + C_{11} \dot{e}_{11} \qquad (12)$$

and

$$\dot{\sigma}_{22} = -C_{22} \frac{\sigma_{22}}{H e^{-b \ln \dot{e}_{eq}}} + C_{22} \dot{e}_{22}, \qquad (13)$$

respectively. It is important to highlight that all the elastic and viscous properties of the lamina are present and coupled in equations (12) and (13).

The lamina elastic constants, C_{ij}, and the constants related to the viscous response, H, b and η_{max}, were recovered via the minimization of the squared differences between the experimental and the model predictions. Thus, the minimizing function was set as

$$R = \sum_{LC,CL,LR} \left[\sum_{v_j} \left(\dot{\sigma}_{exp} - \dot{\sigma} \right)^2 \right]^2 + w \sum_{LC,CL,LR} \left[\sum_{v_j} \left(e_{exp} - e \right)^2 \right]^2, \qquad (14)$$

where the summations over LC, CL and LR stands for the three specimen types and summation over v_j stands for the three crosshead velocities. The weighting constant was chosen $w = E_{11}/\Delta t$, where $\Delta t = 0.125\ s$ was the sampling interval. The evaluation of R for the complete set of results involved around 380,000 data points. The function R was minimized using the optimization software AMPL/Minos [26]. The resulting estimations for the material constants are presented in Table 1.

4. Discussion

The values of the constitutive material constants estimated in Section 3.4 are verified by comparison with the experimental results. In what respect to the elastic response, the constants in Table 1 are replaced into equation (6) to compute the compliance tensor in the lamina coordinate system, D', which is inverted to obtain the stiffness tensor, C', and then rotated using equation (7) to refer it to the tube reference system. The resulting stiffness tensor in the tube reference system is

$$C = \begin{bmatrix} 3.211 & 1.226 & 2.346 & 0 & 0 & 0.444 \\ 1.226 & 4.851 & 1.153 & 0 & 0 & -0.915 \\ 2.346 & 1.153 & 3.275 & 0 & 0 & 0.342 \\ 0 & 0 & 0 & 0.862 & -0.057 & 0 \\ 0 & 0 & 0 & -0.057 & 0.461 & 0 \\ 0.444 & -0.915 & 0.342 & 0 & 0 & 1.260 \end{bmatrix} [GPa]. \qquad (15)$$

It can be observed that, when compared to the experimental values reported in Section 2.2.1, the difference in C_{11} is 27%, while

Table 1
Estimated constitutive constants of the lamina.

E'_{11} [GPa]	4.53
E'_{22} [GPa]	1.54
G'_{12} [GPa]	0.87
v'_{12}	0.2
v'_{23}	0.7
H [MPa s]	1260
b	0.72
η_{max} [MPa s]	10^7

for C_{22} it is only 3.2%.

The Poisson's ratios can be computed as follows

$$\nu_{13} = -\frac{D_{13}}{D_{11}} = 0.63, \qquad (16)$$

$$\nu_{12} = -\frac{D_{12}}{D_{11}} = 0.16 \qquad (17)$$

and

$$\nu_{21} = -\frac{D_{21}}{D_{22}} = 0.38. \qquad (18)$$

The above results are included in Figs. 4–6. It can be observed that there is a good agreement between the computed and experimental values. Deviations between the computed values and the average values of the experimental records are around 15% for the three Poisson's ratios.

The experimental data and the model predictions for the loading/unloading cycles are compared in Figs. 7 and 8 for the longitudinal and circumferential specimens, respectively. It can be observed that model captures the material anisotropic response. With the only exception of the LC specimen with crosshead velocity $v = 0.1$ mm/min, maximum stresses and strains are predicted very accurately. The model predictions for the LC specimens present similar deviations from the experiments in the loading and unloading portions of the curve. On the other hand, the predictions for the CL specimens fit better for the loading portion of the curve. It can be observed from Fig. 8 that the deviations of the model predictions from the experiments are important for the final strain after complete unloading; the model overestimates the experimental measurements by a factor of around 2.4. The above results put in evidence the anisotropic nature of the material viscoplastic behavior.

Among the available options to compute the material constants (this is, to add or remove data from the least-square fitting of R in equation (16) in order to better fit the loading, unloading or both portions of the curves), it was preferred in this work to give priority to the loading, as it better conforms to the intended application in next section.

Finally, we check the fitting for the linear relationship between the stress rate and the stress. To this end, the model predictions are added into Figs. 9 and 10. It can be observed that the model provides reasonable fittings of the experimental data. Maximum deviations occur at low stress levels.

Based on the above observations, it can be concluded that the proposed viscoelastic model has the ability to capture the main features of the material behavior and that it has been properly set-up using the experimental data. The performance of the model is validated in next section via the finite element modeling of an application example.

5. Full-scale tests of a tube

A three-point-bending test of a fiber-reinforced tube was performed to validate the model. The tube data is given in Table 2. Note that the dimensions of the tube are different to those of the tube used to extract the specimens for the material characterization. The experimental setup is depicted in Fig. 12, while schematics of the tests are given in Fig. 13.

The punch load was applied at the tube mid-length via a punch and a hydraulic jack. The load was applied at a constant rate $\dot{P} = 60\ N/s$ during 900 s. Three deflectometers were instrumented: two at the top to monitor the vertical displacement of the punch

Table 2
Tube data.

External diameter, [mm]	Length [mm]	Wall thickness [mm]	Number of laminas	Lamina stacking sequence
541	1900	16	3	$[-82°,+82°,-82°]$

Fig. 12. Actual picture of the bending test used for validation.
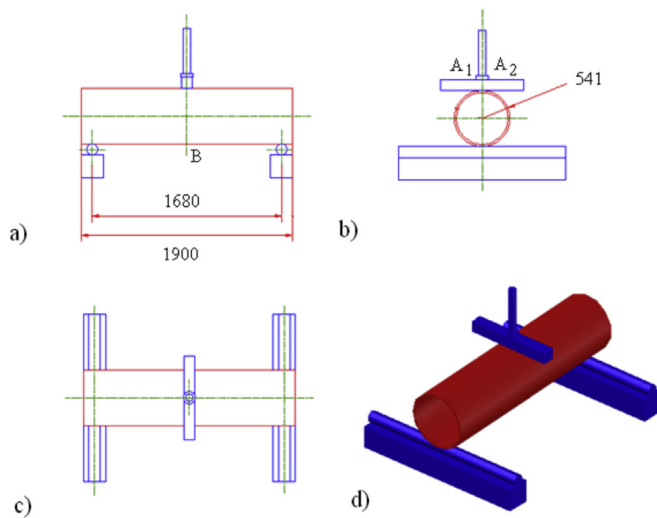
Fig. 13. Schematics of the bending test: a) front, b) side, c) top and d) isometric views. Dimensions are in mm.

(see positions A_1 and A_2 in Fig. 12), and one at the bottom to monitor vertical displacement of the tube outer wall (see position B in Fig. 12). The double measurement of the punch displacement is intended to check the correct horizontal alignment of the punch.

The time evolution of the punch force and the displacements are plot in Fig. 14. The three discontinuities in the curves are due to the stops done to adjust the measuring range of the deflectometers. The measurements recorded by both deflectometers at the top are almost coincident, what indicates the correct alignment of the test. On the other hand, the marked difference between the readings by the of the top and bottom deflectometers puts in evidence that predominant deformation behavior is due to the tube flattening.

The proposed material model was implemented into an in-house developed finite element code, which has been extensively validated in previous engineering applications [25]. The material model was solved via an implicit radial return algorithm written in
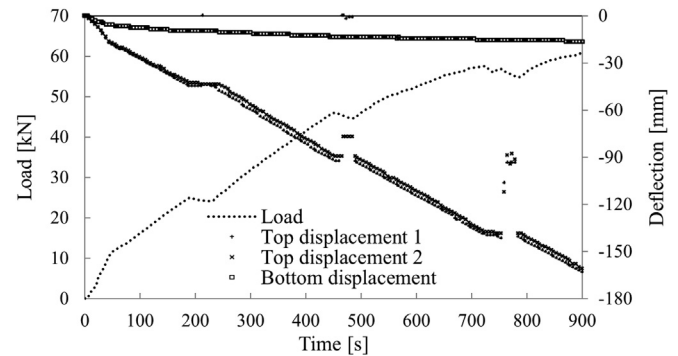
Fig. 14. Experimental results for the time evolution of the load and the tube displacements.

the spatial configuration. The B-bar technique was used to handle the incompressibility associated to the choice of the incompressible-isotropic viscoplastic Newton flow for the trilinear hexahedra elements. This is a standard approach to deal with iso-choric models, and it actually means that the hydrostatic part of viscoelastic stress tensor is controlled by the finite elements and the boundary conditions instead of the constitutive model.

The tube material was modeled as homogenous, with the elastic properties computed as follows:

$$\mathbf{C} = \frac{1}{3} \sum_{i=1}^{3} \mathbf{C}^i, \tag{19}$$

where $\mathbf{C}^i$ are the stiffness matrix of the individual laminas expressed in the tube reference system.

The problem geometry and boundary conditions are symmetric, but the elastic material behavior is not because of the lamina stacking angles, see Table 2. However, preliminary analysis performed using symmetric (one quarter of the problem geometry) and complete models exhibited virtually the same responses. This suggested that the deviation from symmetry of the laminate elastic response have negligible effects on the results of interest for this study. Thus, in order to reduce the computational cost, only one quarter of the tube geometry was modeled by applying the appropriate boundary conditions over the symmetry planes.

The punch displacement was imposed according to the time-history measured in the experiment. One hundred 10-s load increments were used with this purpose.

The results of preliminary simulations showed that friction does not play a significant role, and so, frictionless contact conditions were specified at the punch-tube and support-tube interfaces. For simplicity, perfectly rigid behaviors were assigned to the punch and the support. The contact algorithm involves the use of non-conforming discretizations to effectively account for the large relative tangential displacements between the contacting surfaces, a continuous search for potential contact regions, and the computation of the nodal contact forces via a penalty formulation that enforces the impenetrability condition [25].

The tube was discretized using 8-node isoparametric hexahedral elements, while the contact interfaces were discretized using 4-node quadrilaterals. The mesh was refined in the zones where

the largest strain gradients developed. As a result of a convergence analysis, a mesh with 14,400 elements was used to retrieve the results. This mesh has three elements in the direction of the tube thickness and it is illustrated in Fig. 15.

Fig. 15b show the contours for the equivalent viscous deformation and the von Mises stress at the final deformed configuration. The equivalent viscous deformation contours were computed via the time integration of

$$\dot{e}_{eq}^{v} = \frac{\boldsymbol{\sigma} : L_{v}(\boldsymbol{e}^{v})}{\sigma_{eq}}. \tag{20}$$

It can be observed that the deformation is highly localized in the punch-loading zone. This is coherent with the flattening effect mentioned early.

Fig. 16 compares experimental and FEA results for the time evolution of the punch load. It can be observed that both curves are nearly coincident up to 240 s. Then, after the first relaxation, the model underestimates the load; whereas after the second relaxation, the model has a stiffer response, what inverts the tendency. The two sets of results are nearly coincident by the time of the third relaxation. It is noteworthy that although the above variations, the difference between the two sets of results never exceeds 12%.

Fig. 17 compares experimental and FEA results for the punch load in terms of the vertical displacement. In this case, there is a very good agreement between the two sets of results up to the 45-mm displacement; this is when the first relaxation occurred. From this point on, and in agreement with the behavior observed in Fig. 16, the model predicts a lower force because of the underestimation of the material stiffness. Finally, this trend is inverted when the third relaxation takes place and the model overestimates the material stiffness. The maximum difference between the two sets of results is 15%, and it occurs at the maximum load.

Finally, the equivalent strain and strain rate were monitored at two points: below the punch and at the location of the maximum strain; these positions are labeled A and B, respectively, in Fig. 15a. The results are plot in Figs. 18 and 19. It can be observed that although both points attain similar deformation levels, the deformation rate at point B nearly doubles that of A. The deformation rate at B rapidly increases during the second part of the test due to the flattening of the tube. The results in these plots allow verifying that neither the strain nor the strain rate attain values beyond the range used for the development of the material model.

The results of this study show that the proposed constitutive model is effective to simulate the mechanical behavior of the tubes under monotonic loading conditions. Consequently it might be
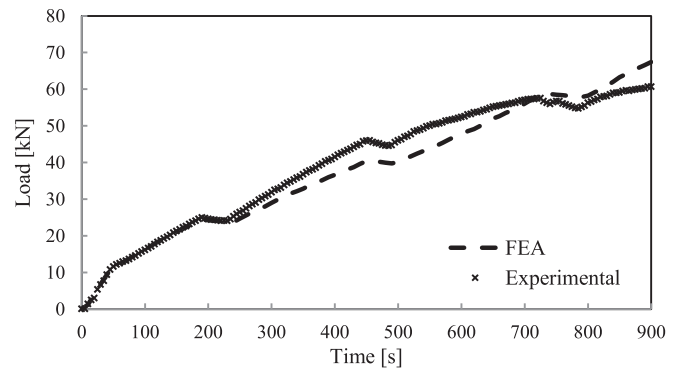

Fig. 16. Experimental and FEA results for the time evolution of the punch load.
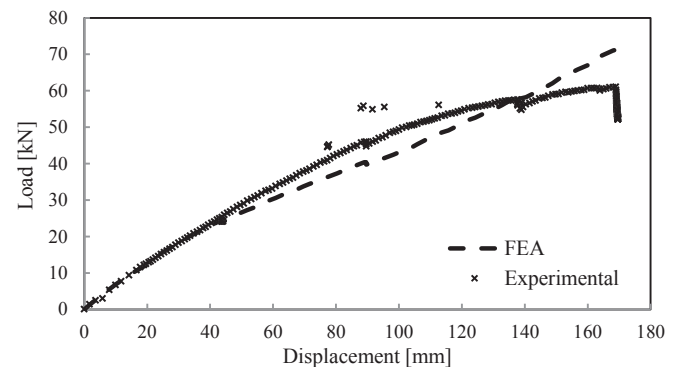

Fig. 17. Experimental and FEA results for the punch load versus vertical displacement.
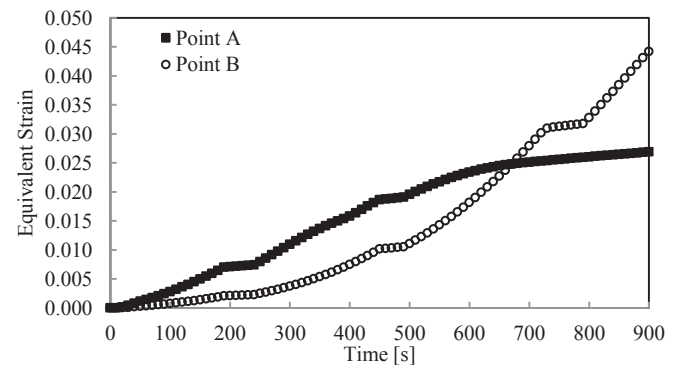

Fig. 18. Deformation histories for a point (A) below the punch and (B) at the location that attains the maximum strain.

used for the analysis of practical situations like those associated with the tube stacking, transport and in-situ assembly.

6. Conclusions

This paper addresses the characterization of the mechanical response of short-fiber reinforced thermoplastic tubes. The tubes are manufactured by helical winding of a composite made of high-density polyethylene (HDPE) with short glass-fibers as reinforcement. The mechanical behavior of the composite lamina was characterized by means of monotonic and loading/unloading tensile tests at different deformation rates. The tests were performed on specimens extracted in the axial and circumferential directions of the tube.
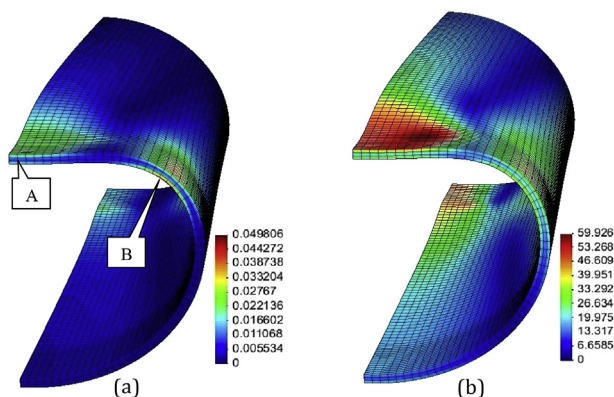

Fig. 15. Deformed finite element discretization with the contour plots for the (a) viscous deformation and (b) von Mises stress for the final deformed configuration (900 s).
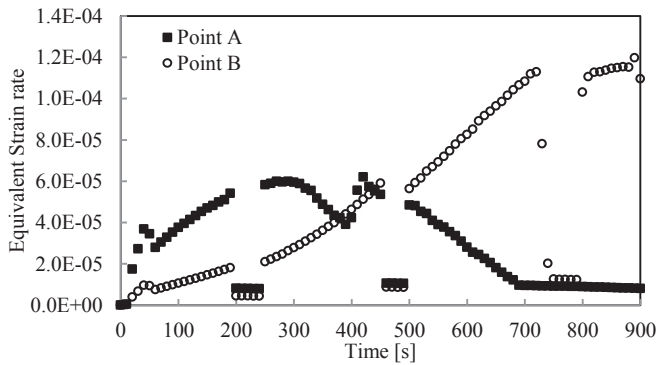
Fig. 19. Deformation-rate histories for a point (A) below the punch and (B) at the location that attains the maximum strain.

The tests allowed observing that the material presents a visco-elastic behavior. The elastic response is transversally isotropic, with the isotropy plane perpendicular to the direction of the fibers; the hysteresis effect diminishes with the strain-rate; and the hysteresis is larger in the transversal than in the longitudinal direction. There are, for all the range of deformation strains studied, acceptable linear correlations between the stress and the stress-rate, and a linear ln–ln correlation between the viscosity and the total strain-rate.

Based on the experimental results, a three-dimensional Maxwell model is proposed for the laminas. The model is tailored to account for the elastic anisotropy of the material while the viscous behavior is defined via a non-linear isotropic law written in terms of the strain-rate. This resultant model has eight parameters (five for the elastic response and three for the viscous response), which are retrieved from the test data via a least square fitting.

The comparison of the model results to the experimental data shows that: the model predictions for the elastic specimen stiffness is very accurate (differences around 3%) in the circumferential direction (this is the direction nearly coincident with the direction of the fibers) but there are important deviations (around 27%) for the longitudinal direction. The predictions of the Poisson's ratios are good; discrepancies between the model predictions and the test data are around 15%. The model properly captures the non-linear anisotropic material response under loading conditions; maximum loads are predicted accurately. For the unloading conditions, the model properly predicts the material response in the longitudinal direction, but it results in important deviations from the experimental measurements in the circumferential direction. These results put in evidence the anisotropic nature of the material viscoplastic behavior and thus provide valuable hints for the further development of the model.

The model for the material behavior is validated by comparison to experimental measurements for a full-scale test that combines the bending and punching of a tube. To this end, the material model was implemented as part of an in-house developed finite element code. The results compare well in terms of forces and displacements. Maximum discrepancies are around 15%. These discrepancies are mainly attributed to the deficiencies of the model to accurately reproduce the material behavior during unloading.

The non-linear characterization of the mechanical response of a short-fiber reinforced polyethylene tube introduced in this work is a step forward with respect to classical linear-elastic analyses. The model has been developed bearing in mind the ease of application for industrial problems. The model has the capability to capture the main features of the material behavior under monotonic loading conditions, it can be set-up using data from tensile tests, and it is compatible for the implementation into standard finite element codes.

References

[1] G. Kalaprasad, K. Joseph, S. Thomas, Theoretical modelling of tensile properties of short sisal fibre-reinforced low-density polyethylene composites, J. Mater. Sci. 32 (1997) 4261–4267.
[2] S. Fu, B. Lauke, E. Mäder, C. Yue, X. Hu, Tensile properties of short-glass-fiber- and short-carbon-fiber-reinforced polypropylene composites, Compos. Part A Appl. Sci. Manuf. 31 (10) (2000) 1117–1125.
[3] P.V. Joseph, G. Mathew, K. Joseph, S. Thomas, P. Pradeep, Mechanical properties of short sisal fiber-reinforced polypropylene composites: comparison of experimental data with theoretical predictions, J. Appl. Polym. Sci. 88 (3) (2003) 602–611.
[4] A.G. Facca, M.T. Kortschot, N. Yan, Predicting the tensile strength of natural fibre reinforced thermoplastics, Compos. Sci. Technol. 67 (2007) 2454–2466.
[5] M.A. Islam, K. Begum, Prediction models for the elastic modulus of fiber-reinforced polymer composites: an analysis, J. Sci. Res. 3 (2) (2011) 225–238.
[6] S. Fu, B. Lauke, Effects of fiber length and fiber orientation distributions on the tensile strength of short-fiber-reinforced polymers, Compos. Sci. Technol. 56 (10) (1996) 1179–1190.
[7] S. Fu, B. Lauke, The elastic modulus of misaligned short-fiber-reinforced polymers, Compos. Sci. Technol. 58 (3–4) (1998) 389–400.
[8] A.F. Hamed, M.H. Megat, S.M. Sapuan, B.B. Sahari, Theoretical analysis for calculation of the through thickness effective constants for orthotropic thick filament wound tubes, Polym. Plast. Technol. Eng. 47 (10) (2008) 1008–1015.
[9] S.V. Thiruppukuzhi, C.T. Sun, Models for the strain-rate-dependent behavior of polymer composites, Compos. Sci. Technol. 61 (1) (2001) 1–12.
[10] V. Oshmyan, S. Patlazhan, Y. Remond, Principles of structural-mechanical modeling of polymers and composites, Polym. Sci. Ser. A 48 (9) (2006) 1004–1013.
[11] K. Chung, H. Ryou, Development of viscoelastic/rate-sensitive-plastic constitutive law for fiber-reinforced composites and its applications. Part I: theory and material characterization, Compos. Sci. Technol. 69 (2) (2009) 284–291.
[12] J. Fritsch, S. Hiermaier, G. Strobl, Characterizing and modeling the non-linear viscoelastic tensile deformation of a glass fiber reinforced polypropylene, Compos. Sci. Technol. 69 (14) (2009) 2460–2466.
[13] A. Andriyana, N. Billon, L. Silva, Mechanical response of a short fiber-reinforced thermoplastic: experimental investigation and continuum mechanical modeling, Eur. J. Mech. A Solids 29 (6) (2010) 1065–1077.
[14] Krah Chile, http//:www.krah.cl.
[15] L. Avérous, J.C. Quantin, A. Crespy, D. Lafon, Evolution of the three-dimensional orientation distribution of glass fibers in injected isotactic polypropylene, Polym. Eng. Sci. 37 (2) (1997) 329–337.
[16] R.J. Crowson, M.J. Folkes, P.F. Bright, Rheology of short glass fiber-reinforced thermoplastics and its application to injection molding I. fiber motion and viscosity measurement, Polym. Eng. Sci. 20 (14) (1980) 925–933.
[17] ASTM D638, Standard Test Method for Tensile Properties of Plastics. Annual Book of ASTM Standards, American Society for Testing and Materials, Philadelphia, 1997, pp. 46–54.
[18] C. Eberl, Digital Image Correlation and Tracking, Matlab Central, 2010. Available at: http://www.mathworks.com/matlabcentral/fileexchange/12413-digital-image-correlation-and-tracking.
[19] P. Bing, Q. Kemao, X. Huimin, A. Anand, Two-dimensional digital image correlation for in-plane displacement and strain measurement: a review, Meas. Sci. Technol. 20 (6) (2009).
[20] P.-C. Hung, A.S. Voloshin, In-plane strain measurement by digital image correlation, J. Braz. Soc. Mech. Sci. Eng. 25 (2003) 215–221.
[21] B. Pan, A. Asundi, H. Xie, J. Gao, Digital image correlation using iterative least squares and pointwise least squares for displacement field and strain field measurements, Opt. Lasers Eng. 47 (2009) 865–874.
[22] O.I. Okoli, G.F. Smith, The effect of strain rate and fibre content on the Poisson's ratio of glass/epoxy composites, Compos. Struct. 48 (1) (2000) 157–161.
[23] M. Schoßig, C. Bierögel, W. Grellmann, T. Mecklenburg, Mechanical behavior of glass-fiber reinforced thermoplastic materials under high strain rates, Polym. Test. 27 (7) (2008) 893–900.
[24] W. Wang, G. Makarov, R.A. Shenoi, An analytical model for assessing strain rate sensitivity of unidirectional composite laminates, Compos. Struct. 69 (1) (2005) 45–54.
[25] D. Celentano, D. Rosales, J. Peña, Simulation and experimental validation of tube sinking drawing processes, Mater. Manuf. Process. 26 (05) (2011) 770–780.
[26] R. Fourer, D. Gay, W. Kernighan, AMPL: a Modeling Language for Mathematical Programming, Thomson Publishing Company, Danvers, MA, USA, 1993.